Cover Page

GOES-R land surface products at Western Hemisphere eddy covariance tower locations

Danielle Losos[1] (losos@wisc.edu, @DanielleLosos), Sophie Hoffman[2] (shoffman22@wisc.edu), Paul C. Stoy[2,3] (pcstoy@wisc.edu, @paulstoy)

Affiliations

1. Space Sciences and Engineering Center (SSEC), University of Wisconsin – Madison, Madison, WI, USA
2. Department of Biological Systems Engineering, University of Wisconsin – Madison, Madison, WI, USA
3. Department of Atmospheric and Oceanic Sciences, University of Wisconsin – Madison, Madison, WI, USA

The following manuscript has been submitted to *Scientific Data* for peer review.

Title

GOES-R land surface products at Western Hemisphere eddy covariance tower locations

Authors

Danielle Losos[1], Sophie Hoffman[2], Paul C. Stoy[2,3]

Affiliations

1. Space Sciences and Engineering Center (SSEC), University of Wisconsin – Madison, Madison, WI, USA
2. Department of Biological Systems Engineering, University of Wisconsin – Madison, Madison, WI, USA
3. Department of Atmospheric and Oceanic Sciences, University of Wisconsin – Madison, Madison, WI, USA

corresponding author(s): Danielle Losos (losos@wisc.edu)

Abstract

The terrestrial carbon cycle varies dynamically over short periods that can be difficult to observe. Geostationary ("weather") satellites like the Geostationary Environmental Operational Satellite - R Series (GOES-R) deliver near-hemispheric imagery at a ten-minute cadence, and its Advanced Baseline Imager (ABI) measures visible and near-infrared spectral bands that can be used to estimate land surface properties and carbon dioxide flux. GOES-R data are designed for real-time dissemination and are difficult to link with eddy covariance time series of land-atmosphere carbon dioxide exchange. We compiled time series of GOES-R land surface attributes including visible and near-infrared reflectances, land surface temperature, and downwelling shortwave radiation (DSR) at 314 ABI fixed grid pixels containing eddy covariance towers. We demonstrate how to best combine satellite and in-situ datasets and show how ABI attributes useful for carbon cycle science vary across space and time. By connecting observation networks that infer rapid changes to the carbon cycle, we can gain a richer understanding of the processes that control it.

Background & Summary

The terrestrial carbon cycle responds to environmental variability, ecological processes like succession, and anthropogenic management at time scales from millennia (or longer)[1] to minutes (or shorter)[2]. Extreme events[3,4], phenological shifts[5], and land management can impact ecosystem carbon cycling on sub-daily time scales, as can variability in solar radiation which largely determines daily carbon dioxide flux if other environmental factors are not limiting[6,7]. These limitations can emerge dynamically as the day progresses if, for example, high temperatures[8], vapor pressure deficit[9], or plant hydrologic functions[10] induce stomatal closure or compromise the photosynthetic machinery. Observing the carbon cycle and the variables that affect it over the time scales at which they covary is critical for understanding the dynamics of the earth system.

Polar-orbiting satellites have return intervals on time scales of days or longer to create data products with time steps of days to years[11,12], limiting our ability to observe the land surface on sub-daily intervals[13]. Geostationary satellites provide real-time observations on time scales of minutes (or less[14]), and host radiometers that measure visible and infrared wavelengths[15,16] which are key for understanding carbon cycle processes[13,17]. These shortwave reflective bands allow us to track key variables including the normalized difference vegetation index (NDVI) commonly used to estimate the leaf area index[17–19] and the near infrared reflectance of vegetation[20] (NIRv: NDVI multiplied by near infrared reflectance) which is strongly linked to ecosystem carbon uptake via gross primary productivity GPP (ref. 21–23), especially when multiplied by incident radiation to derive the NIRvP (ref. 21). Geostationary satellite data have also long been used to estimate terrestrial evapotranspiration[24] to which the carbon cycle is coupled[25], and to create products for key variables that drive carbon cycle processes including downwelling shortwave radiation (DSR) (refs. 26–28) and land surface temperature (LST) (ref. 29,30).

Information from the Geostationary Environmental Operational Satellite - R Series (GOES-R) satellites is created and distributed by the U.S. National Oceanic and Atmospheric Administration (NOAA) in near-real time for weather forecasting and public awareness of critical meteorological events. The ecosystem-atmosphere exchange of carbon dioxide is commonly measured using the eddy covariance technique to create time series of variables like GPP that can extend years or decades into the past. Most eddy covariance towers are managed by individual laboratories as opposed to a coordinated entity, and therefore contain measurements that are often processed and published according to the personal schedule of each tower manager. This makes it difficult for eddy covariance towers to deliver real-time information. In other words, there is a temporal mismatch between eddy covariance and geostationary satellite data dissemination that needs to be addressed to link these rich time series. In addition, the file structures of these two data records are not inherently compatible. While the flux tower observations are time-series by nature, GOES-R data is catalogued as individual raster image files, with hundreds of new files produced every day. To convert a stack of images into a single-pixel time series, every file at each respective timestamp must be read to extract the observation at that one pixel.

The purpose of the present analysis is to bridge this gap by creating time series from GOES-R data products at 314 eddy covariance tower locations from the AmeriFlux and NEON tower networks[31,32]. By providing geostationary satellite data in the same format, file type, and time step as eddy covariance data, we hope that the flux community finds benefit from geostationary satellite data and the geostationary satellite community finds new ways to create products of interest to land surface science. We first describe the Advanced Baseline Imager (ABI) and key land surface products generated by NOAA from its imagery, then explain the Ameriflux and NEON networks and their data structure. We then provide examples of how to best connect “hypertemporal” observations of land surface attributes from satellites with time series of micrometeorological observations including eddy covariance measurements of carbon dioxide flux.

Methods

The GOES-R Series Advanced Baseline Imager (ABI)

The ABI is the primary Earth-observing sensor aboard GOES-R[15,16]. The four satellite GOES-R Series began in November 2016 with the launch of GOES-16. GOES-16 has remained in the GOES-East position ever since. GOES-17 served as GOES-West starting in 2018, however a cooling issue on its loop heat pipe caused partial loss of imagery, and it was replaced by GOES-18 in 2022 (ref [33]). The final satellite in the GOES-R Series is scheduled to launch in 2024 after which point a new series of satellites will be launched by the GeoXO mission[34]. GOES-East and GOES-West orbit at approximately 35,000 kilometers above the equator at 75.2 and 137.2 degrees West. Together they view the entire Western Hemisphere, from eastern Africa to Australia and from Alaska to Chile[35].

The ABI is a passive radiometer that scans the atmosphere, oceans, and Earth surface at sixteen discrete wavelengths ranging from visible to thermal infrared. In its current operational mode (Mode 6), the ABI produces a full disk hemispherical image every ten minutes, a CONUS (Continental United States) or PACUS (Pacific U.S.) image every five minutes, and two mesoscale images per minute. Mesoscale regions are small movable domains that can provide detailed temporal coverage of regions with heightened meteorological interest[16]. Twelve of the sixteen ABI bands have two kilometer spatial resolution at the sub-satellite point (nadir). The shortwave bands 1, 3 and 5 have one-km resolution, while band 2 has 0.5-km resolution [35].

ABI Fixed Grid

Due to the geostationary orbit of GOES satellites, their position and viewing geometry relative to the Earth's surface is, ideally, unchanging. The ABI fixed grid represents each spatial domain (full disk, CONUS/PACUS, and mesoscale) as a grid of ABI scan angles which describe the North/South and East/West orientation of the ABI scan mirrors for every pixel. For each spatial resolution, any two adjacent pixels have equal angular separation. In other words, scan angles remain constant across the fixed grid[16]. However, pixel surface area increases moving away from nadir because a constant scan angle corresponds with greater distance as the earth curves away from the sub-satellite point. While a 2-km GOES-East ABI pixel is 4 km^2 at nadir, the pixel area stretches to 7.2 km^2 near Madison, Wisconsin and 14.3 km^2 near Seattle, Washington (near the furthest extent of the L2 BRF product for GOES-16) as demonstrated in Figure 1.

To accurately map eddy covariance tower locations onto the ABI fixed grid and obtain ABI observations, we needed to align the ABI and tower location information. For GOES-R Level 1b and most Level 2 products, geographic information for each data file is stored as horizontal (x) and vertical (y) scan angles. Converting tower geodetic latitude and longitude coordinates to ABI scan angle coordinates is necessary, as described in the equations in the Appendix (A1 - A7). The following Earth model constants are defined by the Geodetic Reference System 1980 (GRS 80) ellipsoid: the Earth's semi-major axis (r_{eq}), semi-minor axis (r_{pol}) and eccentricity (e, ref. [36]). The satellite's longitude (λ_0) is constant, while targets on the Earth's surface are described by their longitude (λ), latitude (φ), and elevation (z) (ref. [36]). For many earth science applications, the opposite conversion–scan angles to geodetic coordinates–is necessary to geolocate pixels on the Earth surface (Appendix A8 - A15).

ABI fixed grid products are not terrain-corrected: there is no adjustment for the off-nadir view angle of the satellite relative to surface targets. The "parallax effect" causes the satellite to perceive high-elevation targets to be displaced from their true location[37] by a distance that increases with target's elevation and satellite view zenith angle (VZA) as described in Figure 2. GOES satellites only have a nadir view of equatorial surface targets at the sub-satellite points (75.2 °W and 137.2 °W); all other regions require terrain-correction for proper geolocation of elevated targets. Since the present research is concerned with the eddy covariance towers at point locations, it is only necessary that the correct ABI pixel is matched with the targeted tower. The true tower location is shifted by the magnitude and direction of the parallax displacement to the location where it is perceived to be by the ABI fixed grid (see "Corrected Lat/Lon" in Table A1), before the tower is matched with an ABI pixel.

Calculating the perceived tower location takes advantage of the aforementioned conversion from tower geodetic coordinates to ABI scan angles. Typically, this conversion assumes that the geocentric distance (r_c) between the center and the surface of the Earth is equal to the modeled earth radius in GRS 80 (ref. [38]). In addition, our calculation accounts for increased geocentric distance to a target above sea-level. Therefore, the eddy covariance tower site's elevation (z, see ref. 39) is added to r_c.

ABI Level 2 (L2) Products

ABI scans the full disk in under ten minutes, data are processed, and individual netCDF (.nc) files for each data product are made available in near-real time. Most ABI products are created every time a full-disk and CONUS scan is completed, but others currently have less frequent refresh rates, such as once per hour[16]. Here we describe the ABI products that we have compiled for flux tower locations.

L2 Cloud and Moisture Imagery (CMI)

CMI provides reflectance values or brightness temperatures at sixteen ABI channels. The primary data source for this product is the Level 1b (L1b) Radiance product, measuring solar radiation (in W m^{-2} sr^{-1}) at all sixteen ABI bands[35]. For the six reflective bands (Bands 1-6), radiance values are converted to a dimensionless reflectance factor ranging from 0 to 1 by multiplying by the incident Lambertian equivalent radiance (κ)

$$\kappa = \frac{\pi d^2}{E_{sun}} \tag{1}$$

where d is the instantaneous Earth-Sun distance in Astronomical Units and E_{sun} is the solar irradiance in the respective bandpass (W m^{-2} μm^{-1}) as described in the GOES-R Product User Guide (PUG) Volume 5 (ref. 38).

CMI reflectances are considered top-of-atmosphere (TOA) rather than surface reflectances because they measure the total reflectance received by the satellite at the top of the atmosphere, without accounting for atmospheric scattering. For the ten emissive bands (7-16), L1b radiances are converted to brightness temperature (K) using Planck's function[38]. While these longer wavelength measurements are not directly used to measure vegetation, they provide critical atmospheric and environmental context such as characterizing clouds, aerosols, fire, and snow that are of importance for terrestrial carbon cycle science[40].

Bidirectional Reflectance Factors

The L2 bidirectional reflectance factor (BRF) product has been an operational ABI product since August 18, 2021, and provides surface reflectances as a byproduct of the L2 Land Surface Albedo (LSA) product[41]. The LSA algorithm derives Bidirectional Reflectance Distribution Function (BRDF) parameters, which are used to both estimate broadband albedo and to simulate surface reflectance on cloudy days when it cannot be measured directly. Solving for BRDF parameters is accomplished by minimizing a cost function which relates TOA reflectances and Atmospheric Optical Depth (AOD, ref. 42), both of which can be computed from ABI measurements over the course of the day as the solar zenith angle changes.

The BRF algorithm has two paths available for deriving surface reflectances depending on whether clear-sky observations are available. The default and more accurate method, the R3 algorithm, assumes the surface is Lambertian and directly calculates surface reflectance (r_s) from TOA reflectances (r) and atmospheric parameters[41]. Transmittance (γ), and path reflectance (r_0) and spherical albedo (ρ) are retrieved from a look-up table which pre-calculates these parameters given viewing geometry and AOD using the radiative transfer model MODTRAN[43] (Equation 2).

$$r_s = \frac{r - r_0}{\gamma + (r - r_0)\,\rho} \tag{2}$$

$$BRF = \pi BRDF \tag{3}$$

A back-up method is necessary for cloudy conditions where the atmospheric parameters are not available. The R2 algorithm is used to calculate surface BRF from the BRDF parameters retrieved from the prior day's TOA reflectance measurements (Equation 3) to model BRF throughout the day given satellite and solar viewing geometries. Every BRF pixel is tagged with a data quality flag noting whether the R2 or R3 algorithm was used. Another data quality flag indicates the pixel's level of cloudiness, ranging from clear sky, to low, medium or high probability cloudiness (see *Clear Sky Ma*sk). We demonstrate examples of these two methods in *Usage Notes*.

Data availability is limited spatially and temporally because the BRF algorithm is dependent on viewing geometry. The algorithm is not run when either the sun or satellite stray significantly from the zenith, the highest point in the sky relative to the surface target. The VZA of a geostationary satellite to a target on the surface does not change, hence the geographical range where data gets processed is always limited to VZA < 70 degrees. This range is smaller than other full-disk ABI products. For example, the GOES-16 full disk BRF product is valid across most of the continental United States, but excludes the northwestern US, Alaska, and central-northwestern Canada (Figure 3). Solar zenith angle (SZA) varies throughout the day and the algorithm only runs when SZA < 67 degrees. In the Northern Hemisphere winter, when the sun is low in the sky and daylight is short-lived, BRF data are limited to a few mid-day measurements and at high latitudes, the months of December and January have no valid BRF measurements. Inversely, long summer days at high latitudes result in more BRF measurements due to the advantageous sun angles. Near the equator, the number of BRF measurements per day is much less variable.

Land Surface Albedo

The Land Surface Albedo (LSA) product is produced in harmony with the BRF land surface reflectance product. Instantaneous broadband albedo is ideally derived from the clear-sky TOA reflectances and the prior day's BRDF parameters, which in turn are estimated from aerosol optical depth, a daily stack of shortwave reflectances, and albedo climatology[42]. The LSA product is limited by the same viewing geometry restrictions as the BRF product.

Downward Shortwave Radiation (DSR)

The Downward Shortwave Radiation (DSR) product measures the total instantaneous shortwave irradiance incident at the Earth's surface integrated over visible and infrared wavelengths (0.2 to 4.0 µm, ref. [28]). DSR consists of both direct and diffuse solar radiation, attenuated and scattered by the atmosphere, in W m^{-2}. The DSR product is currently produced just once per hour at full disk and CONUS domains. A unique aspect of this L2 product is that DSR data is projected onto a Global Latitude and Longitude Grid, rather than the ABI Fixed Grid used for all other products discussed here (see Converting between projections, Appendix).

Land Surface Temperature

Land Surface (Skin) Temperature (LST) records the instantaneous temperature of the Earth's surface in degrees Kelvin[45,46]. The LST product can only be produced under clear-sky conditions, hence cloud-obstructed observations are masked out. Like DSR, LST is also produced just once per hour. For this reason, LST and DSR were upsampled to match the half-hourly cadence of most Ameriflux time-series, and interpolated values are noted in the data files. The half-hour timestamp values were filled using cubic interpolation between consecutive existing LST observations.

Clear Sky Mask

The Clear Sky Mask, also called the Cloud Mask, provides a binary image with each pixel classified as either "clear" or "cloudy"[47]. First, the algorithm employs spectral, spatial and temporal tests on each pixel to categorize the pixel as "clear", "probably clear", "probably cloudy" and "cloudy." Classifications are compared to the model outputs from the Community Radiative Transfer Model (CRTM, ref. 48). The four-class Cloud Mask intermediate product is a critical input to many other ABI L2 product algorithms, however the four classes are condensed into a binary mask before the final product is distributed to users.

Aerosol Detection Product

The Aerosol Detection Product (ADP) consists of three separate variable layers, each of which is a binary mask representing 'yes detection' or 'no detection'[49]. The three types of aerosol detections are dust, smoke, and aerosols generally (when either dust or smoke has been detected). There are two distinct ADP algorithm pathways for observations over land and ocean, but both begin by masking out high and optically thick clouds. Notably, an ADP product data quality flag denotes "invalid detection due to snow_ice_clouds", information retrieved from the GOES L2 Snow/Ice product, which can be used as a proxy for masking out snow surface cover in other products.

Aerosol Optical Depth

The Aerosol Optical Depth (AOD) product retrieves aerosol optical thickness over both land and ocean[50,51]. Specifically, AOD measures the extinction of solar radiation due to atmospheric aerosols at a wavelength of 550 nm. In addition, the product provides the aerosol particle size, as represented by two Ångström exponents. The algorithm relies on instantaneous TOA reflectances, and a look-up table of atmospheric parameters precalculated using a radiative transfer model. Different ABI reflectance channels are used for the land and the ocean AOD retrievals. The AOD algorithm relies on the aerosol type characterization generated by the ADP product.

Calculating NIRvP using GOES-R

To calculate NDVI, NIRv and NIRvP on a per-pixel basis, the three inputs required are ABI Band 2 (red) surface reflectance, ABI Band 3 (NIR) surface reflectance, and DSR. These values are retrieved from the L2 BRF and DSR products, respectively, and observations are filtered to remove poor quality observations using the corresponding data quality flags. The NDVI is the normalized difference between the red and NIR (equation 4), which is multiplied by NIR to derive NIRv (equation 5), and is then multiplied by photosynthetically active radiation (PAR) to derive NIRvP (equation 6); both NIRv and NIRvP are strongly related to GPP (refs. [20,52]). A photosynthetically active radiation (PAR) product is scheduled for forthcoming GOES-R data product releases and work is ongoing to provide PAR and DSR across GeoNEX[53]. In the interim, we estimated PAR (in W m^{-2}) as 0.45 times DSR (ref. 54); we note that this will induce a small amount of uncertainty into the final NIRvP estimate as this conversion factor varies depending on atmospheric composition and solar position[54–56].

$$\mathrm{NDVI} = \frac{\mathrm{NIR}-\mathrm{Red}}{\mathrm{NIR}+\mathrm{Red}} \quad (4)$$

$$\mathrm{NIRv} = \mathrm{NDVI} \times \mathrm{NIR} \quad (5)$$

$$\mathrm{NIRvP} = \mathrm{NIRv} \times \mathrm{PAR} \quad (6)$$

The flux community often uses photosynthetically active photon flux density with units of μmol m^{-2} s^{-1}. PAR can be converted to photosynthetically active photon flux density PPFD by using a conversion factor of approximately 4.56 μmol J^{-1} (ref. [57]).

Eddy covariance

The AmeriFlux network relies on the efforts of individual tower operating teams across the Western Hemisphere[31] which, coupled with NEON, Inc. eddy covariance towers, resulted in 314 eddy covariance towers at VZA under 70° with publicly available data at time of writing[39]. These data are collected by the tower-operating teams or NEON, Inc.[32,58] and provide half-hourly (or in rare instances hourly) sums of carbon dioxide, water, sensible heat, and/or other trace gas fluxes and half-hourly (or hourly) averages or sums of micrometeorological variables, all quality control-checked by common algorithms[59,60] and organized as .csv files. These files are updated shortly after new data are uploaded to AmeriFlux or NEON, which in practice may result in delays that can extend from months to years from the time at which data were collected.

Data Records

We created 314 .csv files of GOES-R time series at eddy covariance tower locations (Table A1) on the same half-hourly interval as most eddy covariance observations. To do so, we extracted surface reflectances, cloud and aerosol products, LST and DSR – and associated data quality control flags – from GOES-R files at the 314 eddy covariance tower locations as described in Table 1 for the late August 2021 - December 2022 period for which the GOES-R surface reflectance product is available. Files also include satellite-earth geographic information including view and solar zenith angles and parallax-adjusted geographic coordinates as well as time information in standard UTC units and local standard time, the latter of which is the convention for the eddy covariance data files.

Linking half-hourly averages of micrometeorological variables and surface-atmosphere fluxes with GOES-R full disk scans presents a challenge. The mid-point of the eddy covariance data files are 15 or 45 minutes past the hour and GOES-R scans begin near the top of the hour, then ten, twenty, thirty, forty and fifty minutes afterward for observations that take approximately ten minutes to complete from north to south (Figure 4). In other words, there is not a GOES-R scan that aligns cleanly with the midpoint of the eddy covariance observations. Furthermore, not all of the ABI products are produced as frequently as the scan cadence: DSR and LST are produced just once per hour, at the top of the hour. We upsampled DSR and LST observations to match the half-hour eddy covariance interval by performing cubic interpolation between the hourly data points as noted. When describing the data in *Technical Validation*, we discuss how shifting eddy covariance time series by 15 minutes so that the average of the measurement start and end time approximately matches the GOES-R data that we obtained can improve the time alignment.

Technical Validation

We first demonstrate the relationship between tower-measured and GOES-R estimated DSR and explain how aligning average observation times can be beneficial for interpreting observations. ABI DSR and tower DSR have a strong positive correlation with r = 0.923. However, the ABI DSR product is produced just once per hour, a less frequent cadence than the tower DSR measurements. When ABI and tower DSR are plotted against each other, a hysteresis (hole-like feature in the scatterplot) appears at low to middle DSR values (Figure 5). The time lag between tower and GOES-R observations appears to be the cause (Figure 6). The tower DSR values rise in the morning fifteen minutes before GOES observations, then decline in the afternoon fifteen minutes earlier as well. Interpolating between the hourly DSR observations to half-hourly timesteps (Figure 6B) creates better alignment between the products, increasing the r^2 coefficient from 0.836 to 0.839.

Usage Notes

The data reveal key differences that vary by ecosystem type in variables related to carbon cycling. We first describe patterns that emerge when investigating data from pixels that include all 314 tower sites then describe time series from six different ecosystems that reflect a range of the different ecosystems encountered in the dataset.

Figure 7 illustrates the variability in midday NIRvP across ecosystem types. NIRvP generally increases in the morning and decreases in the afternoon due to the DSR (Figure 6), causing the diurnal peak to occur around midday. The midday NIRvP median between 1000 and 1400 local standard time was computed from half-hourly observations at every site. Then we calculated the mean of the monthly midday medians, creating a summarized chronology of NIRvP behavior at each site over the year (Figure 7A). Deciduous and especially evergreen broadleaf forests have the highest average NIRvP year-round, and barren ecosystems and open shrublands the lowest. Wetland ecosystems have the highest between-site variability in NIRvP. The NIRvP standard deviation (plotting standard deviations of the monthly midday medians, Figure 7B) highlights which land cover types vary most strongly across the data record. The monthly standard deviation in NIRvP tends to be relatively low when its mean is also low. On the other end, croplands and deciduous broadleaf sites have high standard deviation in NIRvP, as expected due to the highly seasonal nature of these vegetation types. More insight into the temporal dynamics of different ecosystem types can be gained by a close examination of representative examples.

Site descriptions for six sample Ameriflux sites

We highlight features of the ABI data from pixels that encompass six representative Ameriflux sites, which we first describe briefly.

BR-CST

Caatinga Serra Talhada (BR-CST) is a tropical dry forest on the far eastern side of Brazil[62]. The vegetation is deciduous needleleaf forest, but open enough to allow for cattle grazing in the wet season. The semi-arid Steppe climate delivers cold winter temperatures. No logging has taken place here for at least 50 years.

PE-QFR

Quistococha Forest Reserve (PE-QFR) is a tropical peatland palm swamp in northeastern Peru[63]. The site is just outside the city of Iquitos in a natural protected forest reserve near the Amazon River. The predominant vegetation is *Mauritia flexuosa*, a wetland palm. The tropical climate here is defined by a long wet season and short dry season from June to August[64].

US-Br1

Brooks Field Site 10-Ames is a cropland that rotates between corn and soy, depending on the year[65]. The site is located in Ames, Iowa, just north of Des Moines in the heart of the Upper Midwest Corn Belt. The humid continental climate is characterized by very cold winters, hot summers, and year-round precipitation. Two additional eddy covariance towers are located at different fields on the same farm named US-Br2 and US-Br-3.

US-CGG

The Concord Grazed Grassland (US-CGG) rangeland is tucked into the suburbs of Concord, California, within the East Bay Area. While the property is part of California State University's East Bay Concord Campus, the grassland is managed by a local rancher who grazes around 60 cattle in the cool season from December to April. During the cool season, temperatures remain mild and annual grasses dominate due to the Mediterranean climate.

US-Cwt

Coweeta (US-Cwt) is a southern Appalachian site at an elevation of 690 meters in western North Carolina near the border with Georgia, near the USFS Coweeta Hydrologic Laboratory[66,67]. This temperate secondary forest is primarily deciduous broadleaf, and the Warm Summer Continental climate exhibits significant rainfall year-round. The forest was logged until the 1930s.

US-Ho1

Howland Forest is an evergreen needleleaf forest in central Maine and the US-Ho1 eddy covariance tower has one of the longest flux records dating back to 1996 (ref. 68). The Howland Research Forest was founded by a partnership between the University of Maine and the International Paper Company. Stands are multi-aged due to its commercial history of logging select species. The forest is dominated by spruce, hemlock and fir and lies at the transition between northeastern deciduous forest and boreal evergreen forest[69]. Two other towers, US-Ho2 and US-Ho3 are also located at Howland Forest.

Individual ABI Band 2 (Red) and band 3 (NIR) surface reflectance measurements over one week in June are demonstrated in Figure 8. Figure 8 makes apparent the variability of clear-sky observations: the signal can be extremely noisy or very smooth depending on the site and date. Compare, for example, the smooth diurnal curves at US-CGG (California) to the jagged spikes at US-Ho1 (Maine). We surmise that the noisy clear-sky time-series are the result of thin undetected clouds and aerosols obscuring the surface reflectance signal. On the other hand, the modeled surface-reflectance measurements under cloudy-sky conditions are relatively smooth. These estimates, however, have more uncertainty especially following long stretches without clear-sky observations because they rely on clear-sky observations to extrapolate the reflectance under the clouds.

The time series of DSR and NIRv over the sixteen-month period for which GOES-R surface reflectance observations were available elucidate site-specific trends in climate and phenology (Figure 9). Fourteen-day moving averages can help encapsulate the signal while demonstrating the intra-daily variability. Equatorial sites (Figure 9a and b) receive more consistent solar radiation year-round, but cloud cover is more likely to interfere during the wet season (May through August) at BR-CST. The wetland PE-QFR is moderated by the (largely) water-saturated soils, causing steadier NIRv – and therefore likely vegetation productivity – than at BR-CST, a tropical dry forest. The other four Northern Hemisphere sites (Figures 9c - 9f) receive higher solar insolation in the summer, but phenological trends are land cover dependent. The evergreen forest (US-Ho1) has higher NIRv on average than the deciduous forest (US-Cwt) which surges in productivity during spring leaf-up and declines during fall senescence; the flat line at US-Ho1 is consistent with missing data due to snow cover. Compared to these natural forests, the corn crop at US-Br1 has a more pronounced and condensed growing season. In the Mediterranean climate of the US-CCG site, the grass NIRv reaches its highest values in the cool winter season.

While Figure 9 demonstrates yearly variability in DSR and NIRv, Figure 10 depicts how NIRvP – the product of these factors with the former adjusted to approximate PAR – fluctuates on average over the course of a single day. Hourly mean NIRvP values are further broken down by month, representing how landscapes exhibit unique diurnal patterns at different times of year. The general form of this pattern is a midday peak in NIRvP due to DSR reaching its peak at the daily solar zenith. July at the US-Br1 cropland (Figure 10c) is a notable exception, likely caused by midday clouds. At the wetland PE-QFR (Figure 10b), the diurnal NIRvP pattern stays consistent between months while the deciduous forests and agricultural field show striking differences between seasons. At a couple sites, the maximum NIRvP does not coincide with solar noon, creating asymmetrical curves. The BR-CST peak shifts towards the afternoon while US-CGG shifts towards the morning (Figure 10a and Figure 10d).

This diurnal asymmetry is driven in part by NIRv, which can be attributed to the site-specific viewing geometry – the site longitude (related to the satellite's VZA) is tightly correlated to diurnal asymmetry (Figure 11). In other words, the further a site is from the GOES-16 sub-satellite point (75.2 degrees East), the more the reflectance peak strays from solar noon. To measure asymmetry, we calculated the diurnal centroid at each site by taking the mean diurnal time weighted by the half-hourly mean NIRvP by month (Equation 7) (ref. 70). Hence, any deviation from 12 (local noon) represents a shift towards the morning or afternoon. Since the majority of our sites are West of GOES-16, it is logical that most sites would have a diurnal centroid under 12 corresponding with a morning shift in peak NIRvP.

$$centroid = \frac{\sum_{t=0}^{24} NIRvP_t \times t}{\sum_{t=0}^{24} NIRvP_t} \tag{7}$$

In summary, GOES-R data can provide rich time series that helps quantify the variability in key land surface attributes that are related to carbon cycling, but the native data format and challenges with parallax and coordinate system rotation has limited its ability to link to surface-atmosphere flux time series like the eddy covariance time series organized by Ameriflux, NEON Inc. and others that are used by the carbon cycle community. By providing GOES-R observations for multiple eddy covariance sites we hope to provide a way forward to better link hypertemporal and sub-daily satellite and eddy covariance observations.

Code Availability

Code is available on Google Colab at:
https://colab.research.google.com/drive/1lgyPhYVXr4MffWnN7m-5Bo3Lt5f4f49D?usp=sharing

Data are currently available at https://portal-s.edirepository.org/nis/mapbrowse?packageid=edi.1420.1

Acknowledgements

Support for this research was provided by the University of Wisconsin - Madison Office of the Vice Chancellor for Research and Graduate Education with funding from the Wisconsin Alumni Research Foundation. We also acknowledge support from the National Science Foundation award 2106012. We are grateful to Sadegh Ranjbar and Ojaswee Shrestha for insightful comments.

Author contributions

DL collected and visualized GOES-R data with assistance from SH who prepared files for submission to the Environmental Data Initiative. DL and PCS wrote the manuscript with assistance from SH.

Competing interests

No competing interests are noted.

Appendix

Converting between projections

The geodetic latitudes and longitudes of Ameriflux towers are converted to ABI scan angles (with a parallax adjustment applied) to geolocate the towers on the ABI Fixed Grid (equations A1 - A7). Other earth science applications will often do the inverse operations to convert the satellite's scan angles to geodetic latitudes and longitudes (equations A8 - A15). The L2 DSR product is not projected on the ABI fixed grid, but instead uses the Global Latitude and Longitude, also known as the equirectangular projection. However, the eddy covariance site geodetic coordinates still must be adjusted to account for the parallax effect. Therefore, the ABI scan angles are computed from the site latitude, longitude and elevation, then converted back to geodetic latitude and longitude, using both sets of equations below (A1 -A15).

The equations below are described in greater detail in the GOES-R PUG Volume 5 (ref. 38), Section 4.2.8 "Navigation of Image Data," pages 21 - 26. Figure 4.2.8 in the PUG illustrates the GRS 80 ellipsoid Earth model and the relationship between the two coordinate frames/projections. In the two sets of equations below, some of the same physical parameters are defined differently depending on which values are unknown (unknowns are either latitude/longitude or ABI scan angles). Please refer to Figure 4.2.8 in ref. 38 for the entire visualization.

Geodetic latitude and longitude to ABI scan angles[38]

The N/S elevation angle (*y*) and E/W scanning angle (*x*) are computed using

$$y = arctan\left(\frac{s_z}{s_x}\right) \quad \text{(A1)}$$

$$x = arcsin\left(\frac{-s_y}{\sqrt{s_x^2+s_y^2+s_z^2}}\right) \quad \text{(A2)}$$

Where

$$s_x = H - r_C cos(\phi_C) cos(\lambda - \lambda_0) \quad \text{(A3)}$$

$$s_y = -r_C cos(\phi_C) sin(\lambda - \lambda_0) \quad \text{(A4)}$$

$$s_z = r_C sin(\phi_C) \quad \text{(A5)}$$

H is the height of the satellite from the center of the Earth (4,2164,160 m), λ_0 is the longitude of the projection origin (−1.309 radians), ϕ is the GRS80 geodetic latitude in radians, λ is the geodetic longitude in radians, the geocentric latitude is:

$$\phi_C = arctan\left(\frac{r_{pol}^2}{r_{eq}^2} tan(\phi)\right) \quad \text{(A6)}$$

And the geocentric distance to the point on the ellipsoid is

$$r_C = \frac{r_{pol}}{\sqrt{1-e^2 cos^2(\phi_C)}} \quad \text{(A7)}$$

ABI scan angles to geodetic latitude and longitude[38]

$$\phi = arctan\left(\frac{r_{eq}^2 s_z}{r_{pol}^2 \sqrt{(H - s_x)^2 + s_y^2}}\right) \quad \text{(A8)}$$

$$\lambda = \lambda_0 - arctan\left(\frac{s_y}{H - s_x}\right) \quad \text{(A9)}$$

Where

$$r_s = \frac{-b - \sqrt{b^2 - 4ac}}{2a} \quad \text{(A10)}$$

In which

$$a = sin^2(x) + cos^2(x)\left(cos^2(y) + \frac{r_{eq}^2}{r_{pol}^2} sin^2(y)\right) \quad \text{(A11)}$$

$$b = -2H cos(x) cos(y) \quad \text{(A12)}$$

$$c = H^2 - r_{eq}^2 \quad \text{(A13)}$$

$$s_x = r_s cos(x) cos(y) \quad \text{(A14)}$$

$$s_y = -r_s sin(x) \quad \text{(A15)}$$

Table A1: The site identifier, tower locations including parallax correction, and climate and ecosystem type of the 314 Ameriflux eddy covariance sites explored here.

GOES_manuscript_sites.csv

Figures

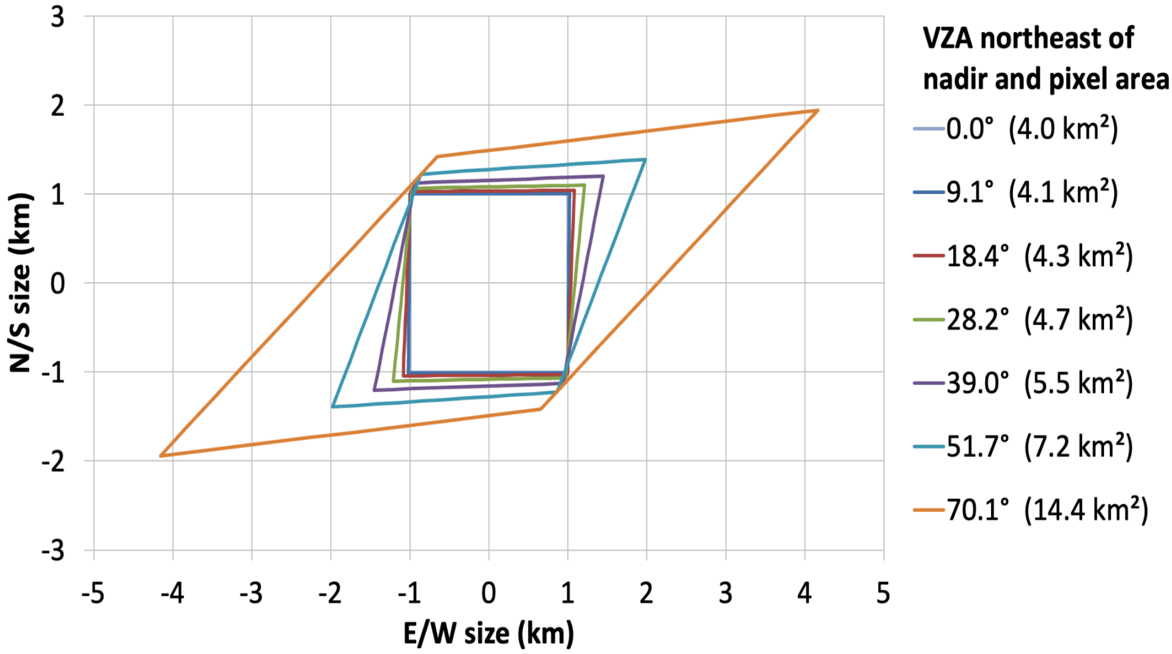

Figure 1

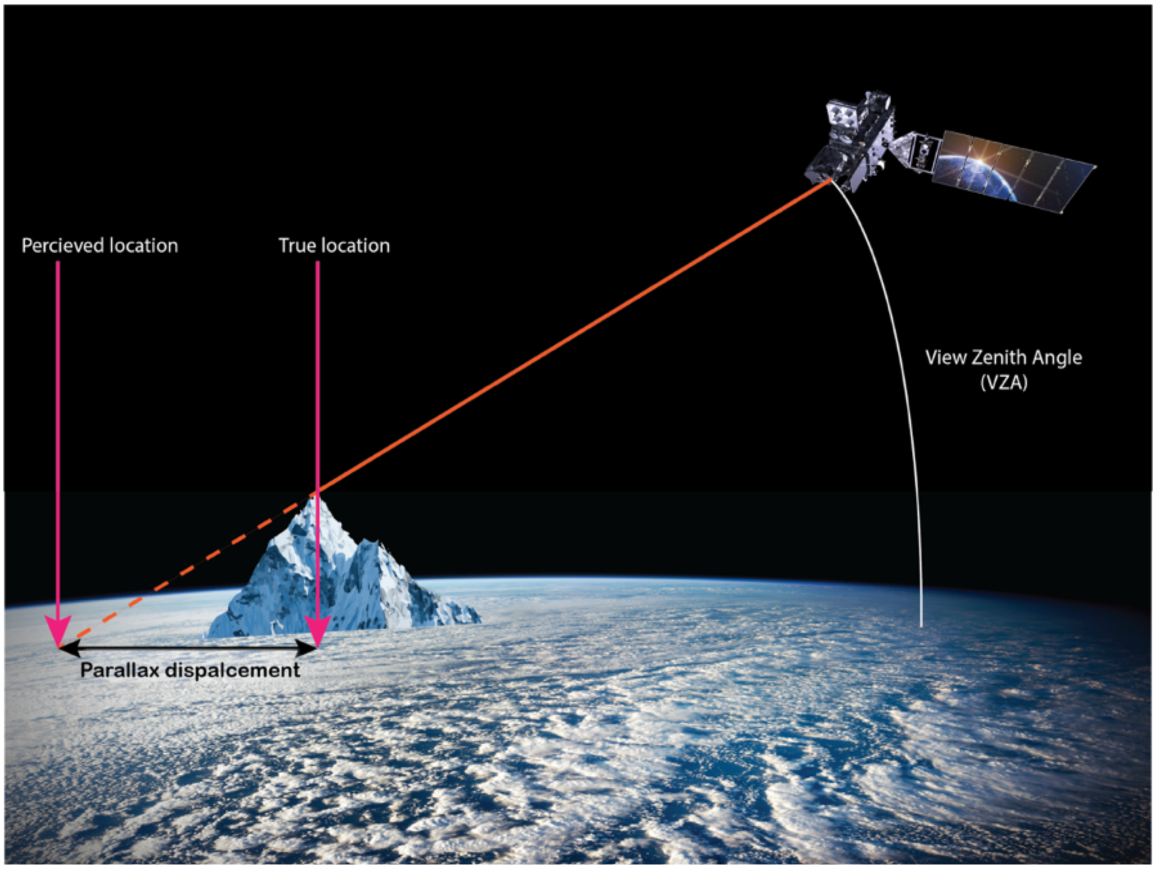

Figure 2


Greenland
Northwestern Passages
NU
Hudson Bay
Labrador Sea
Canada
YT
NT
AK
AB
BC
MB
SK
ON
QC
NL
NB
PE
NS
WA
MT
ND
MN
OR
ID
WY
SD
NE
NV
UT
United States
IL
IN
OH
MI
NY
MO
KY
WV
MD
NC
TN
SC
AR
OK
AZ
TX
LA
MS
AL
GA
North Atlantic Ocean
orth
icific
cean
HI
Gulf of Mexico
Mexico
Cuba
Puerto Rico
Guatemala
Caribbean Sea
Nicaragua
Venezuela
Guyana
Suriname
Colombia
RR
AP
Ecuador
AM
PA
MA
CE
RN
PB
PI
AL
SE
Brazil
AC
Peru
RO
TO
MT
BA
GO
Bolivia
MG
ES
MS
SP
RJ
Paraguay
PR
SC
Chile
RS
Uruguay
Argentina
South Pacific Ocean

Figure 3

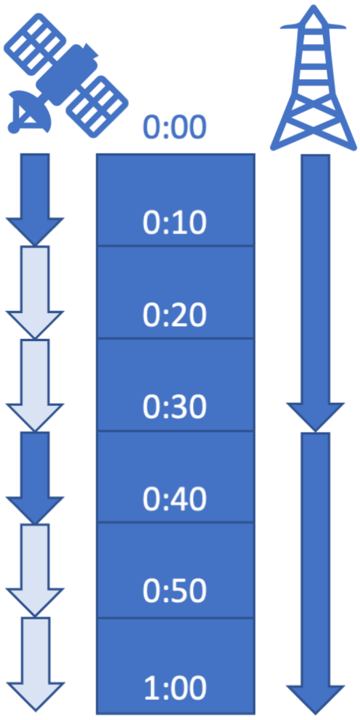

Figure 4

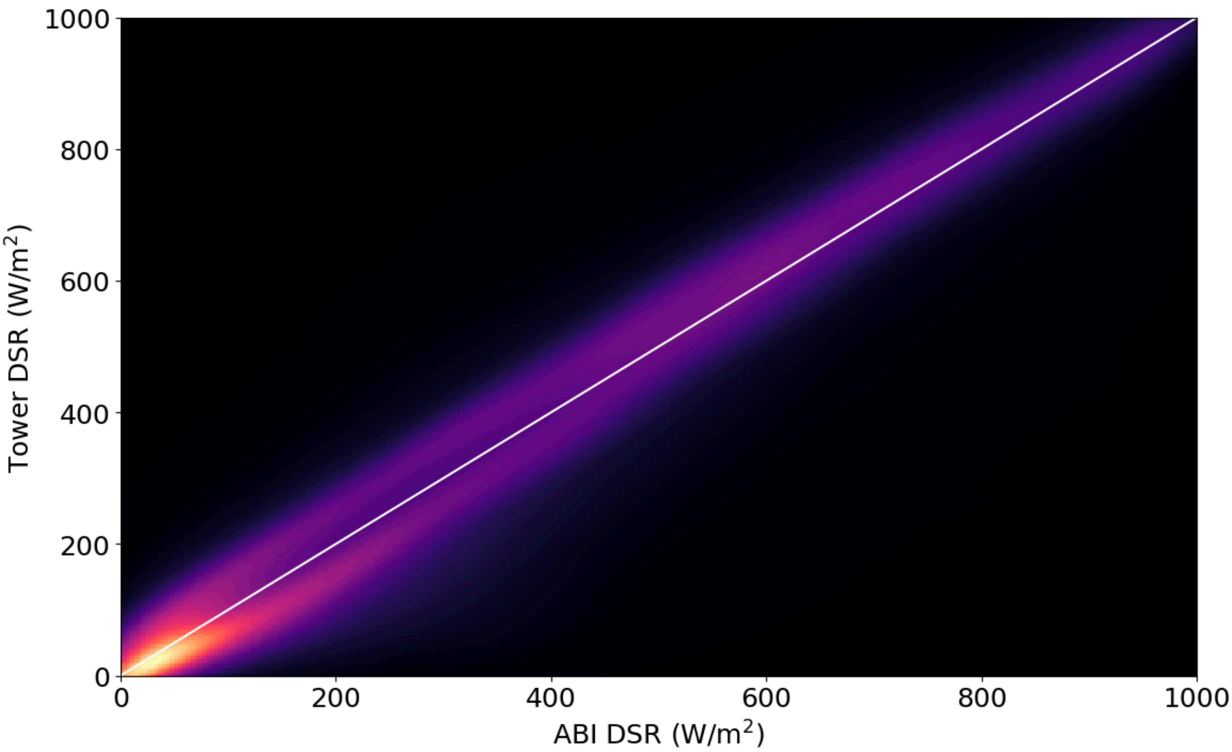

Figure 5

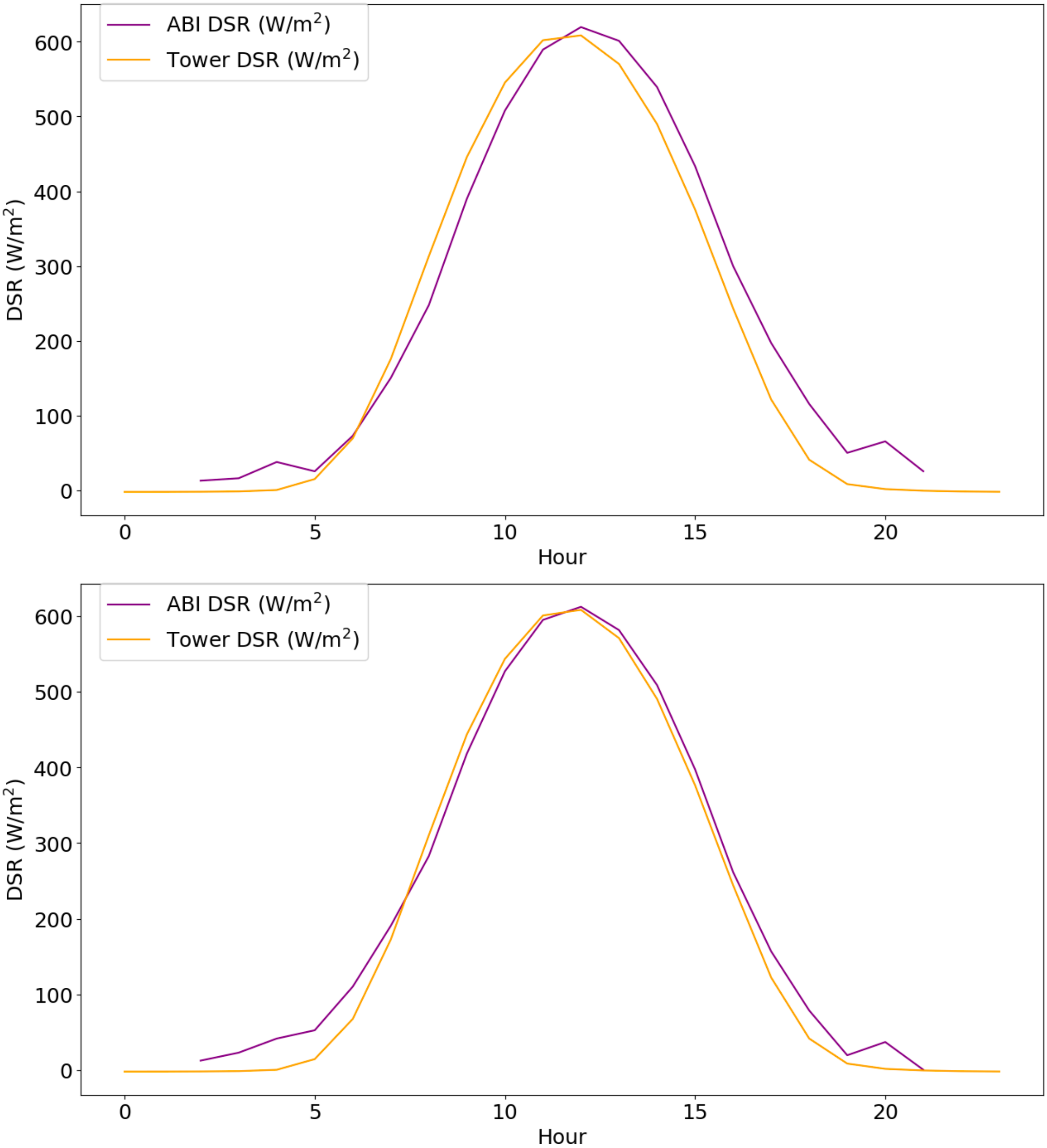
ABI DSR (W/m^2)
Tower DSR (W/m^2)
DSR (W/m^2)
Hour
0
100
200
300
400
500
600
0
5
10
15
20
ABI DSR (W/m^2)
Tower DSR (W/m^2)
DSR (W/m^2)
Hour
0
100
200
300
400
500
600
0
5
10
15
20

Figure 6

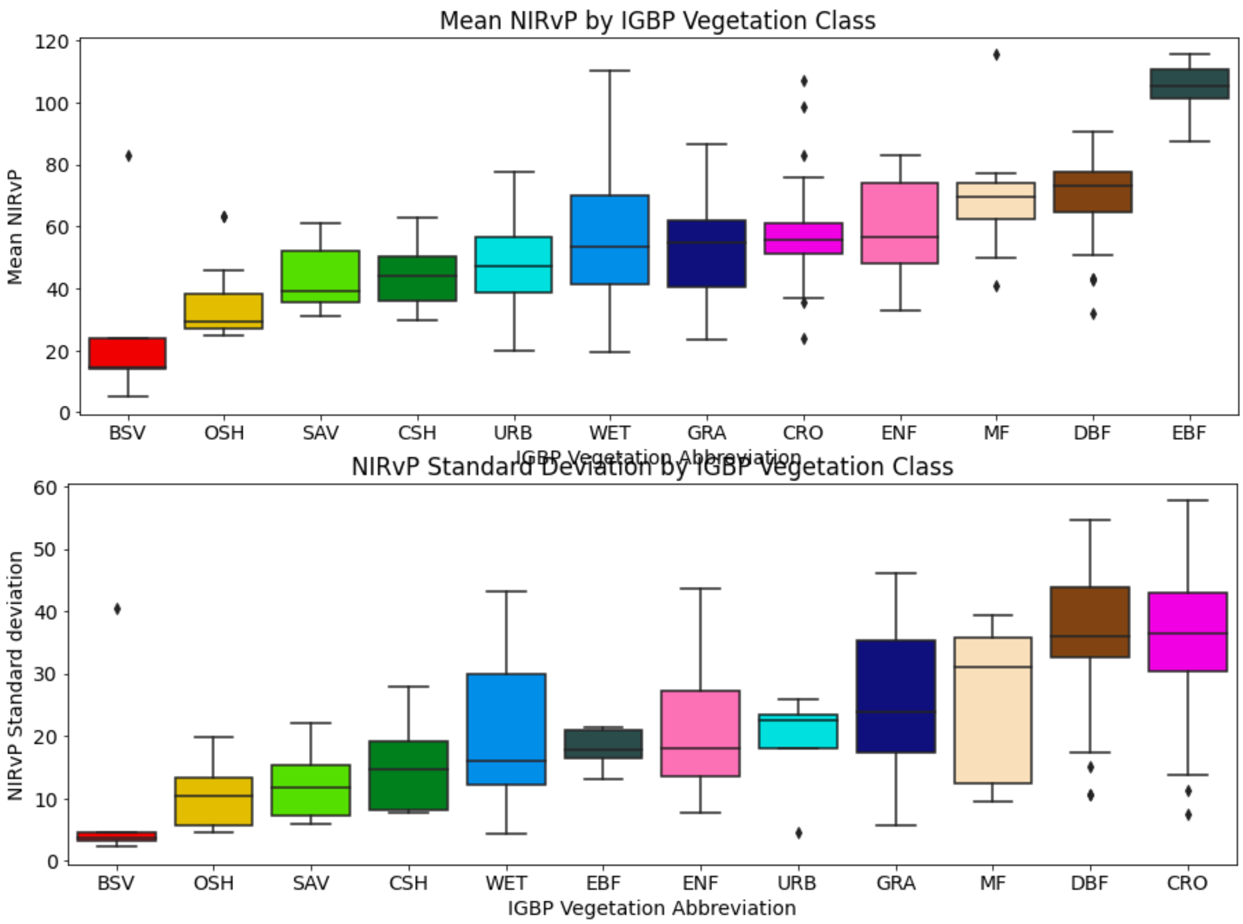
Mean NIRvP by IGBP Vegetation Class
Mean NIRvP
0
20
40
60
80
100
120
BSV
OSH
SAV
CSH
URB
WET
GRA
CRO
ENF
MF
DBF
EBF
IGBP Vegetation Abbreviation
NIRvP Standard Deviation by IGBP Vegetation Class
NIRvP Standard deviation
0
10
20
30
40
50
60
BSV
OSH
SAV
CSH
WET
EBF
ENF
URB
GRA
MF
DBF
CRO
IGBP Vegetation Abbreviation

Figure 7

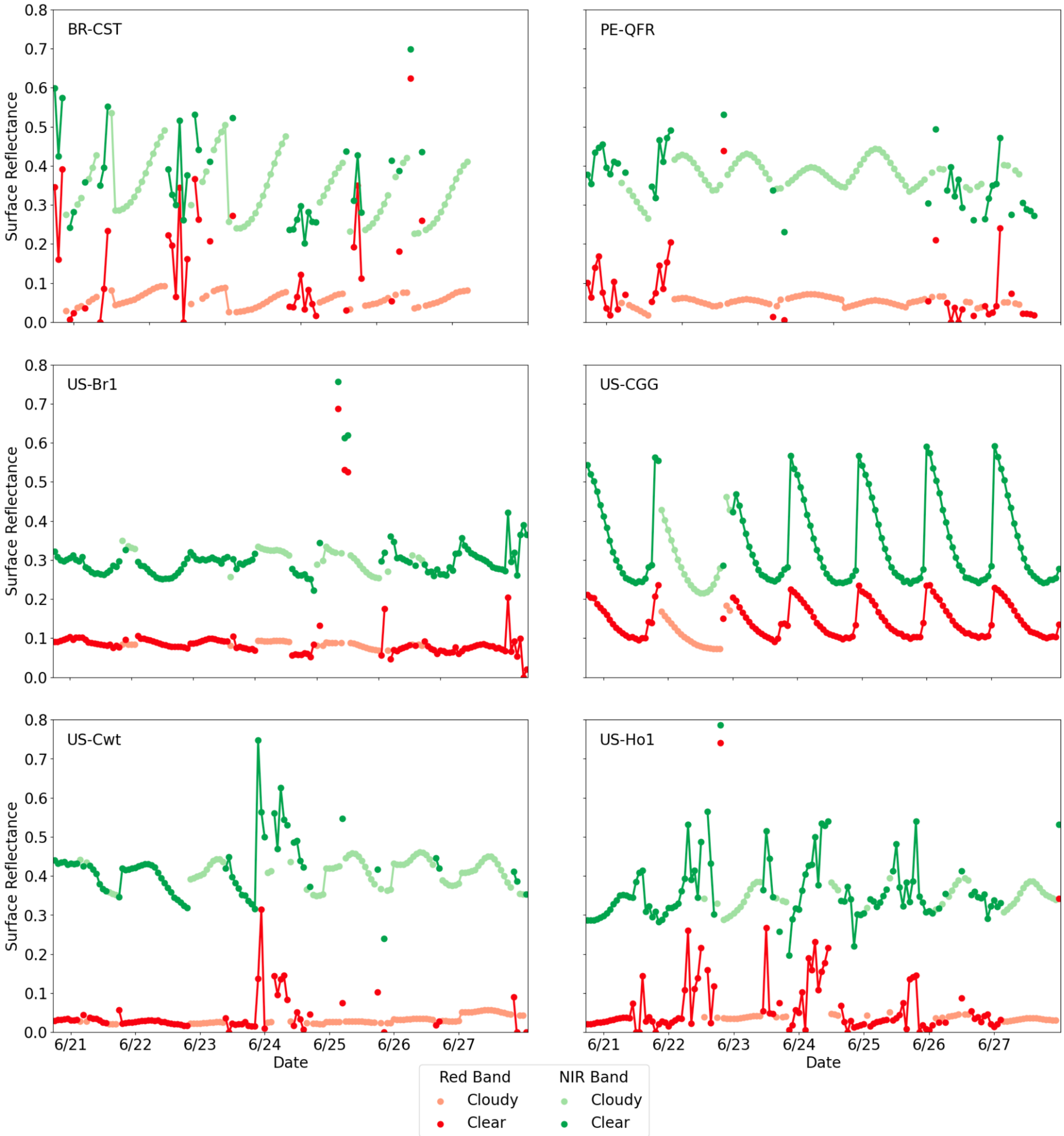

566
567 Figure 8

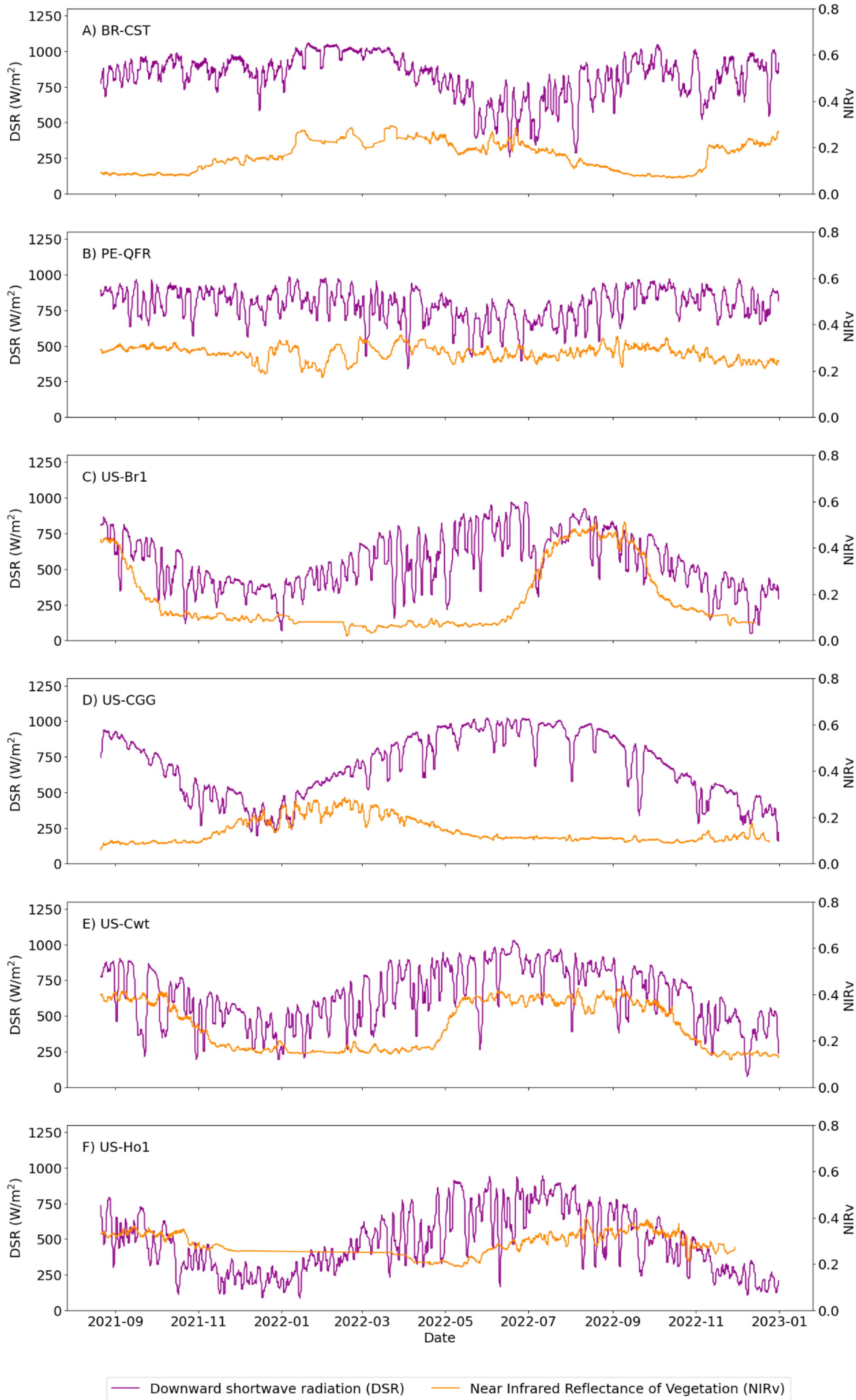
A) BR-CST
B) PE-QFR
C) US-Br1
D) US-CGG
E) US-Cwt
F) US-Ho1
DSR (W/m^2)
NIRv
0
250
500
750
1000
1250
0.0
0.2
0.4
0.6
0.8
2021-09
2021-11
2022-01
2022-03
2022-05
2022-07
2022-09
2022-11
2023-01
Date
Downward shortwave radiation (DSR)
Near Infrared Reflectance of Vegetation (NIRv)

Figure 9

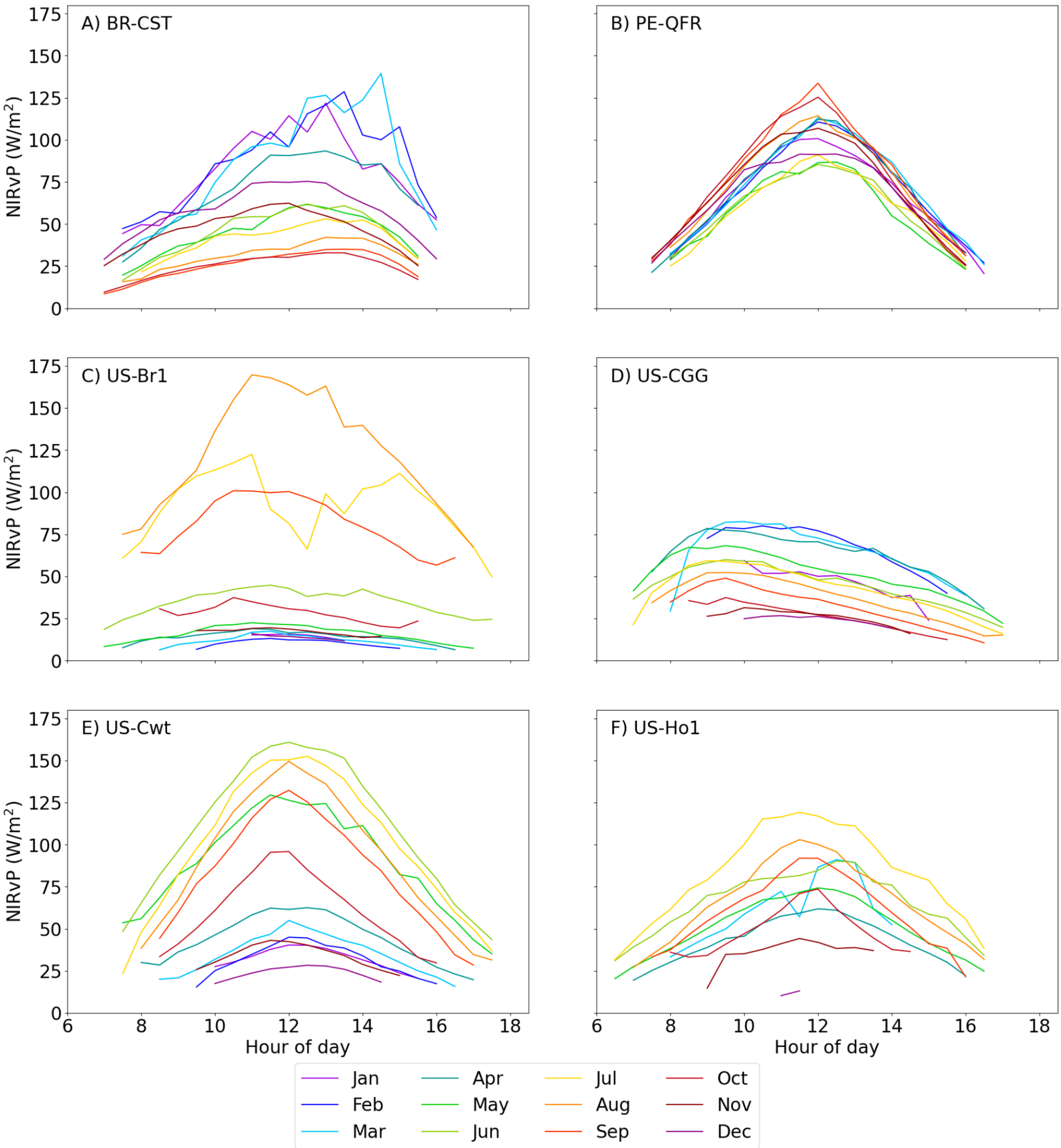

A) BR-CST
B) PE-QFR
C) US-Br1
D) US-CGG
E) US-Cwt
F) US-Ho1
NIRvP (W/m^2)
0
25
50
75
100
125
150
175
6
8
10
12
14
16
18
Hour of day
Jan
Feb
Mar
Apr
May
Jun
Jul
Aug
Sep
Oct
Nov
Dec

Figure 10

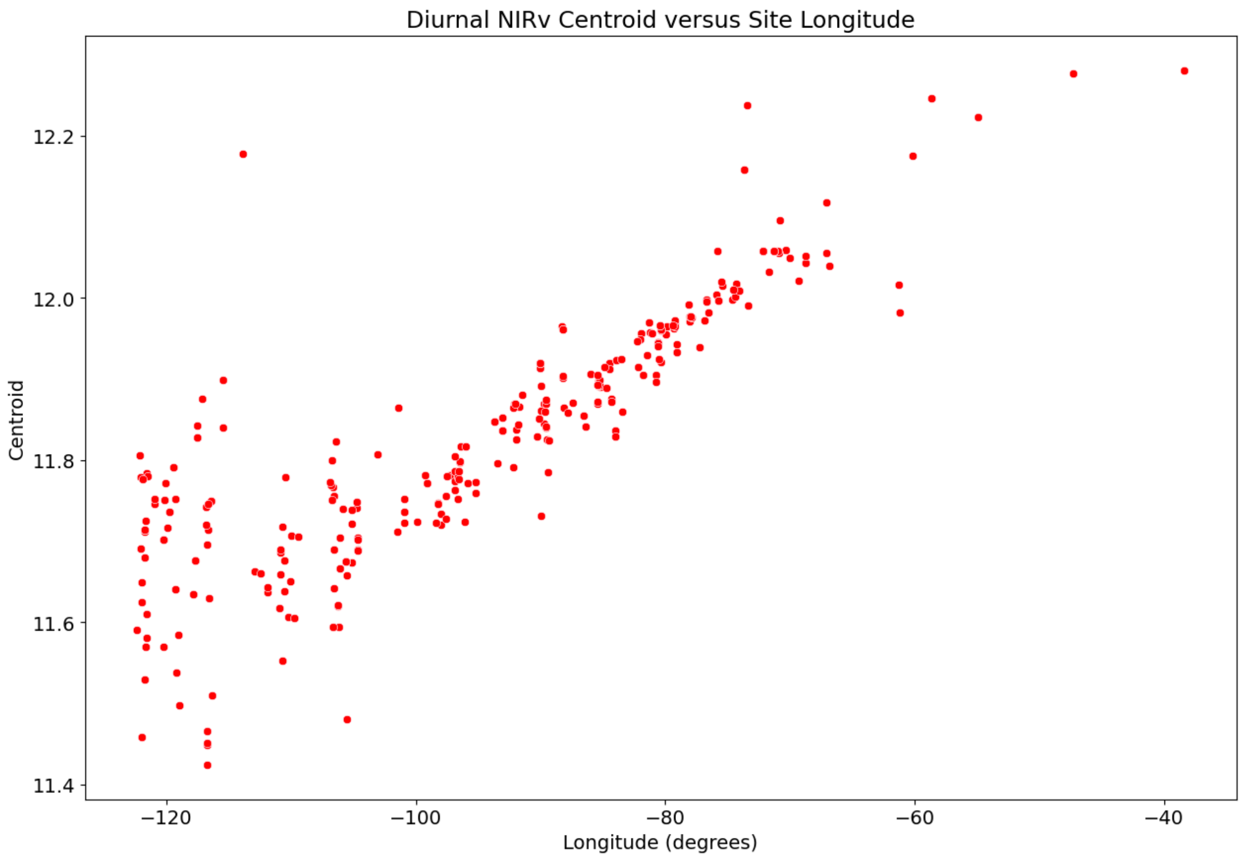

Figure 11

Figure Legends

Figure 1: GOES-R ABI pixel outlines and areas (in km/km^2) at increasing VZA northeast of nadir (in degrees).

Figure 2: A schematic showing how off-nadir view angles can impact the projected locations of elevated surface targets[37].

Figure 3: Ameriflux and NEON, Inc. eddy covariance sites with available GOES-16 L2 bidirectional reflectance factor (BRF) products as black dots and those without available data as red dots, produced in Google Earth Engine[44].

Figure 4: A description of GOES-R Mode 6 full disk timing from the top of the hour (left) that makes a discrete measurement for each pixel scanning from north to south, versus half-hourly eddy covariance data (right) that represent the average or sum of variables measured between a start and end point at the top of the hour and each half hour (or in rare cases hour).

Figure 5: A two-dimensional kernel density ("heat map") representation of downwelling shortwave radiation (DSR) from the Advanced Baseline Imager (ABI) onboard GOES-R versus eddy covariance tower incident shortwave radiation observations ('Tower DSR') for 314 eddy covariance tower sites.

Figure 6: The diurnal course of downwelling shortwave radiation (DSR) from the Advanced Baseline Imager (ABI) onboard GOES-R versus eddy covariance tower incident shortwave radiation observations ('Tower DSR') for 314 eddy covariance tower sites when using the 'start

time' of the eddy covariance measurements (top) versus those after interpolating between hourly ABI DSR observations (bottom).

Figure 7: The mean (top) and standard deviation (bottom) of the midday (1000-1400 local standard time) near infrared reflectance of vegetation multiplied by photosynthetically active radiation (NIRvP; units W m^{-2}) when aggregating GOES-R pixels containing eddy covariance towers by International Geosphere Biosphere Programme (IGBP) vegetation type.

Figure 8: Surface reflectances in the red (ABI Band 2) and near infrared (ABI Band 3) for the six example eddy covariance sites described in the text during a one-week period in June. The hue of observations indicates whether the clear-sky or cloudy algorithm was implemented.

Figure 9: Downward shortwave radiation (DSR) and the near infrared reflectance of vegetation (NIRv) for the six representative Ameriflux eddy covariance tower sites described in the text for the late August 2021 - December 2022 period for which the ABI surface reflectance product was available.

Figure 10: The mean diurnal cycle of GOES-R NIRvP by month for the six representative Ameriflux eddy covariance sites studied here.

Figure 11: The diurnal centroid of NIRvP from GOES-16 for the 314 Ameriflux eddy covariance tower locations described here.

Tables

Table 1. The GOES-R products with variable name, data quality flag, brief description and units that were compiled for eddy covariance tower locations.

GOES-R Series Products				
Cloud and Moisture Imagery	CMI_C01	DQF_C01	Top of Atmosphere Reflectance - Band 1 (Blue) Ratio between outgoing radiance at one given direction and incoming radiance at another given direction (same or different from the incoming direction) at the top of the atmosphere.	Unitless factor from 0 to 1
	CMI_C02	DQF_C02	Top of Atmosphere Reflectance - Band 2 (Red)	
	CMI_C03	DQF_C03	Top of Atmosphere Reflectance - Band 3 (NIR)	
Bidirectional Reflectance Factor	BRF1	BRF_DQF	Surface Reflectance - Band 1 (Blue) Ratio between outgoing radiance at one given direction and incoming radiance at another given direction (same or different from the incoming direction) at the Earth's surface.	Unitless factor from 0 to 1
	BRF2		Surface Reflectance - Band 2 (Red)	
	BRF3		Surface Reflectance - Band 3 (NIR)	
Land Surface Albedo	LSA	LSA_DQF	Ratio between outgoing and incoming irradiance at the Earth's surface.	Unitless factor from 0 to 1
Clear Sky Mask	ACM	ACM_DQF	Binary mask indicating a medium or high probability of cloud in the pixel.	
Aerosol Optical Depth	AOD	AOD_DQF	The extinction of solar radiation due to atmospheric aerosols at a wavelength of 550 nm.	Dimensionless quantity
Aerosol Detection Product	ADP_aero	ADP_DQF	Binary mask that signals the presence of any aerosols in the pixel.	Dimensionless quantity (0 or 1)

	ADP_smk		Binary mask that signals the presence of smoke aerosols in the pixel.	
	ADP_dust		Binary mask that signals the presence of dust aerosols in the pixel.	
Land Surface Temperature	LST	LST_DQF	Instantaneous land surface skin temperature.	Degrees Kelvin
Downward Shortwave Radiation	DSR	DSR_DQF	Instantaneous total shortwave irradiance (flux) received at the Earth's surface integrated over the 0.2 to 4.0 um wavelength interval.	W/m^2
Derived Products				
Normalized Difference Vegetation Index	NDVI	N/A	Normalized difference between red and near-infrared reflectance (ABI Bands 2 and 3).	Unitless factor from -1 to 1
Near Infrared Reflectance of Vegetation	NIRv	N/A	NDVI multiplied by near-infrared reflectance (ABI Band 3).	Unitless factor from -1 to 1
Photosynthetically Active Radiation	PAR	N/A	Approximated by multiplying DSR by 0.45	W/m^2
NIRv multiplied by PAR	NIRvP	N/A	NIRv multiplied by incoming sunlight (PAR)	W/m^2
Viewing Geometry				
Solar Azimuth Angle	SAA	N/A	Horizontal angle between a ray from the site to polar north, and the solar ray.	Degrees
Solar Zenith Angle	SZA	N/A	Vertical angle between a tangent normal to the site surface, and the solar ray.	Degrees
Solar Position	SOLAR_POS	N/A	Unique solar position defined as the sum of the SZA and SAA.	Degrees
Time				
Timestamp	UTC_TIME	N/A	The observation time in Coordinated Universal Time (UTC).	yyyy-mm-dd hh:mm:ss.ms
Local time	LOCAL_TIME	N/A	The observation time in local time relative to where the EC tower site is located.	yyyy-mm-dd hh:mm:ss.ms
Day of year	DOY	N/A	Julian day from 0 to 365 (or 366 on Leap Years)	Unitless
Hour	HOUR	N/A	Hour of day (0 to 23)	Unitless

Constant Variables	Variable Name	Description	Units
Ameriflux Site Information			
Site Id	SITE_ID	Name identification of Ameriflux site	N/A
Timezone	TIMEZONE	Timezone abbreviation and UTC offset from local time	TTT+0
Geodetic coordinates	SITE_LAT, SITE_LON	Ameriflux provided latitude and longitude of site	Degrees
Elevation	ELEVATION	Ameriflux provided elevation of site	Meters
GOES Earth-Satellite Measurements			
View zenith angle	VZA	Angle between the line connecting the satellite to the surface, and the tangent normal to the surface.	Degrees
Parallax displacement	PARALLAX	Displacement of the target location as perceived by the satellite due to off-nadir VZA.	Meters
Geodetic coordinates	CORRECTED_LAT, CORRECTED_LON	False latitude and longitude adjusted to account for parallax displacement.	Degrees

Ecological Information			
Vegetation Type (IGBP)	VEGETATION_IGBP	International Geosphere Biosphere Programme (IGBP) Type 1 land cover scheme identifies 17 land cover classes (0 – 16) which includes 11 natural vegetation classes, 3 developed and mosaicked land classes, and three non-vegetated land classes. [61]	N/A
Climate Class (Köppen)	CLIMATE_KOEPPEN	Classification that divides terrestrial climates into five major types based on seasonal precipitation and temperature patterns. Represented by the letters A, B, C, D, and E.	N/A

References

1. Falkowski, P. *et al.* The global carbon cycle: a test of our knowledge of earth as a system. *science* **290**, 291–296 (2000).
2. Pearcy, R. W., Krall, J. P. & Sassenrath-Cole, G. F. Photosynthesis in fluctuating light environments. *Photosynth. Environ.* 321–346 (1996).
3. Reichstein, M. *et al.* Climate extremes and the carbon cycle. *Nature* **500**, 287–295 (2013).
4. Zscheischler, J. *et al.* A few extreme events dominate global interannual variability in gross primary production. *Environ. Res. Lett.* **9**, 035001 (2014).
5. Piao, S., Friedlingstein, P., Ciais, P., Viovy, N. & Demarty, J. Growing season extension and its impact on terrestrial carbon cycle in the Northern Hemisphere over the past 2 decades. *Glob. Biogeochem. Cycles* **21**, (2007).
6. Stoy, P. C. *et al.* Biosphere-atmosphere exchange of CO_2 in relation to climate: a cross-biome analysis across multiple time scales. *Biogeosciences* **6**, 2297–2312 (2009).
7. Stoy, P. C. *et al.* Variability in net ecosystem exchange from hourly to inter-annual time scales at adjacent pine and hardwood forests: a wavelet analysis. *Tree Physiol.* **25**, 887–902 (2005).
8. Allakhverdiev, S. I. *et al.* Heat stress: an overview of molecular responses in photosynthesis. *Photosynth. Res.* **98**, 541–550 (2008).
9. Novick, K. A. *et al.* The increasing importance of atmospheric demand for ecosystem water and carbon fluxes. *Nat. Clim. Change* **6**, 1023–1027 (2016).
10. Matheny, A. M. *et al.* Characterizing the diurnal patterns of errors in the prediction of evapotranspiration by several land-surface models: An NACP analysis. *J. Geophys. Res. Biogeosciences* **119**, 1458–1473 (2014).
11. Turner, D. P. *et al.* Evaluation of MODIS NPP and GPP products across multiple biomes. *Remote Sens. Environ.* **102**, 282–292 (2006).
12. Running, S. W. & Zhao, M. Daily GPP and annual NPP (MOD17A2/A3) products NASA Earth Observing System MODIS land algorithm. *MOD17 User's Guide* **2015**, 1–28 (2015).
13. Xiao, J., Fisher, J. B., Hashimoto, H., Ichii, K. & Parazoo, N. C. Emerging satellite observations for diurnal cycling of ecosystem processes. *Nat. Plants* **7**, 877–887 (2021).
14. Schmit, T. J. *et al.* Geostationary Operational Environmental Satellite (GOES)-14 super rapid scan operations to prepare for GOES-R. *J. Appl. Remote Sens.* **7**, 073462–073462 (2013).
15. Schmit, T. J. & Gunshor, M. M. ABI imagery from the GOES-R series. in *The GOES-R Series* 23–34 (Elsevier, 2020).
16. Schmit, T. J. *et al.* A closer look at the ABI on the GOES-R series. *Bull. Am. Meteorol. Soc.* **98**, 681–698 (2017).
17. Khan, A. M. *et al.* Reviews and syntheses: Ongoing and emerging opportunities to improve environmental science using observations from the Advanced Baseline Imager on the Geostationary Operational Environmental Satellites. *Biogeosciences* **18**, 4117–4141 (2021).
18. Wheeler, K. I. & Dietze, M. C. Improving the monitoring of deciduous broadleaf phenology using the Geostationary Operational Environmental Satellite (GOES) 16 and 17. *Biogeosciences* **18**, 1971–1985 (2021).
19. Miura, T., Nagai, S., Takeuchi, M., Ichii, K. & Yoshioka, H. Improved characterisation of vegetation and land surface seasonal dynamics in central Japan with Himawari-8 hypertemporal data. *Sci. Rep.* **9**, 1–12 (2019).

20. Badgley, G., Anderegg, L. D., Berry, J. A. & Field, C. B. Terrestrial gross primary production: Using NIRV to scale from site to globe. *Glob. Change Biol.* **25**, 3731–3740 (2019).
21. Dechant, B. *et al.* NIR$_V$P: A robust structural proxy for sun-induced chlorophyll fluorescence and photosynthesis across scales. *Remote Sens. Environ.* **268**, 112763 (2022).
22. Jeong, S. *et al.* Tracking diurnal to seasonal variations of gross primary productivity using a geostationary satellite, GK-2A advanced meteorological imager. *Remote Sens. Environ.* **284**, 113365 (2023).
23. Khan, A. *et al.* The diurnal dynamics of Gross Primary Productivity using observations from the Advanced Baseline Imager on the Geostationary Operational Environmental Satellite-R Series at an oak savanna ecosystem. *J. Geophys. Res. Biogeosciences* **127**, e2021JG006701 (2022).
24. Jacobs, J. M., Myers, D. A., Anderson, M. C. & Diak, G. R. GOES surface insolation to estimate wetlands evapotranspiration. *J. Hydrol.* **266**, 53–65 (2002).
25. Gentine, P. *et al.* Coupling between the terrestrial carbon and water cycles—a review. *Environ. Res. Lett.* **14**, 083003 (2019).
26. Diak, G. R. & Gautier, C. Improvements to a simple physical model for estimating insolation from GOES data. *J. Clim. Appl. Meteorol.* 505–508 (1983).
27. Gautier, C., Diak, G. & Masse, S. A simple physical model to estimate incident solar radiation at the surface from GOES satellite data. *J. Appl. Meteorol. Climatol.* **19**, 1005–1012 (1980).
28. Laszlo, I., Liu, H., Kim, H.-Y. & Pinker, R. T. Shortwave Radiation from ABI on the GOES-R Series. in *The GOES-R Series* 179–191 (Elsevier, 2020).
29. Sims, D. A. *et al.* A new model of gross primary productivity for North American ecosystems based solely on the enhanced vegetation index and land surface temperature from MODIS. *Remote Sens. Environ.* **112**, 1633–1646 (2008).
30. Li, X., Xiao, J., Fisher, J. B. & Baldocchi, D. D. ECOSTRESS estimates gross primary production with fine spatial resolution for different times of day from the International Space Station. *Remote Sens. Environ.* **258**, 112360 (2021).
31. Novick, K. A. *et al.* The AmeriFlux network: A coalition of the willing. *Agric. For. Meteorol.* **249**, 444–456 (2018).
32. Schimel, D., Hargrove, W., Hoffman, F. & MacMahon, J. NEON: A hierarchically designed national ecological network. *Front. Ecol. Environ.* **5**, 59–59 (2007).
33. Pogorzala, D. *et al.* Mitigating the GOES-17 ABI thermal anomaly using predictive calibration. in *Sensors, Systems, and Next-Generation Satellites XXIV* vol. 11530 106–112 (SPIE, 2020).
34. Schmit, T. J. *et al.* US Plans for Geostationary Hyperspectral Infrared Sounders. in 5411–5414 (IEEE, 2022).
35. Schmit, T. J. & Gunshor, M. M. Chapter 4 - ABI Imagery from the GOES-R Series. in *The GOES-R Series* (eds. Goodman, S. J., Schmit, T. J., Daniels, J. & Redmon, R. J.) 23–34 (Elsevier, 2020). doi:10.1016/B978-0-12-814327-8.00004-4.
36. GOES-R Series Product Definition and User's Guide (PUG) Volume 3: Level 1b Products. (2019).
37. Pestana, S. & Lundquist, J. D. Evaluating GOES-16 ABI surface brightness temperature observation biases over the central Sierra Nevada of California. *Remote Sens. Environ.* **281**, 113221 (2022).
38. GOES-R Series Product Definition and User's Guide (PUG) Volume 5: Level 2+ Products. (2019).
39. Stoy, P. C. *et al.* The global distribution of paired eddy covariance towers. *bioRxiv* 2023–03 (2023).
40. Schmit, T. J., Lindstrom, S. S., Gerth, J. J. & Gunshor, M. M. Applications of the 16 spectral bands on the Advanced Baseline Imager (ABI). *J. Oper. Meteorol.* **06**, 33–46 (2018).
41. Yu, Y., Peng, J. & Yu, P. GOES-R Advanced Baseline Imager (ABI) algorithm theoretical basis

document for surface albedo. (2021).

42. He, T., Zhang, Y., Liang, S., Yu, Y. & Wang, D. Developing land surface directional reflectance and albedo products from geostationary GOES-R and Himawari data: Theoretical basis, operational implementation, and validation. *Remote Sens.* **11**, 2655 (2019).
43. Berk, A. *et al.* MODTRAN® 6: A major upgrade of the MODTRAN® radiative transfer code. in 1–4 (IEEE, 2014).
44. Gorelick, N. *et al.* Google Earth Engine: Planetary-scale geospatial analysis for everyone. *Remote Sens. Environ.* (2017).
45. Yu, Y. *et al.* Developing algorithm for operational GOES-R land surface temperature product. *IEEE Trans. Geosci. Remote Sens.* **47**, 936–951 (2008).
46. Yu, Y. *et al.* Validation of GOES-R satellite land surface temperature algorithm using SURFRAD ground measurements and statistical estimates of error properties. *IEEE Trans. Geosci. Remote Sens.* **50**, 704–713 (2011).
47. Heidinger, A. K. *et al.* ABI cloud products from the GOES-R series. in *The GOES-R Series* 43–62 (Elsevier, 2020).
48. Han, Y. JCSDA community radiative transfer model (CRTM): Version 1. (2006).
49. Kondragunta, S., Laszlo, I., Zhang, H., Ciren, P. & Huff, A. Air quality applications of ABI aerosol products from the GOES-R series. *GOES-R Ser.* 203–217 (2020).
50. Zhang, H., Kondragunta, S., Laszlo, I. & Zhou, M. Improving GOES Advanced Baseline Imager (ABI) aerosol optical depth (AOD) retrievals using an empirical bias correction algorithm. *Atmospheric Meas. Tech.* **13**, 5955–5975 (2020).
51. Fu, D., Gueymard, C. A. & Xia, X. Validation of the improved GOES-16 aerosol optical depth product over North America. *Atmos. Environ.* **298**, 119642 (2023).
52. Badgley, G., Field, C. B. & Berry, J. A. Canopy near-infrared reflectance and terrestrial photosynthesis. *Sci. Adv.* **3**, e1602244 (2017).
53. Wang, D. & Li, R. A GeoNEX-based 1km hourly land surface downward shortwave radiation (DSR) and photosynthetically active radiation (PAR) product, Zenodo [data set]. *Zenodo Data Set* **10**, (2022).
54. Britton, C. & Dodd, J. Relationships of photosynthetically active radiation and shortwave irradiance. *Agric. Meteorol.* **17**, 1–7 (1976).
55. Szeicz, G. Solar radiation for plant growth. *J. Appl. Ecol.* 617–636 (1974).
56. Howell, T., Meek, D. & Hatfield, J. Relationship of photosynthetically active radiation to shortwave radiation in the San Joaquin Valley. *Agric. Meteorol.* **28**, 157–175 (1983).
57. Dye, D. G. Spectral composition and quanta-to-energy ratio of diffuse photosynthetically active radiation under diverse cloud conditions. *J. Geophys. Res. Atmospheres* **109**, (2004).
58. Metzger, S. *et al.* From NEON field sites to data portal: a community resource for surface–atmosphere research comes online. *Bull. Am. Meteorol. Soc.* **100**, 2305–2325 (2019).
59. Pastorello, G. *et al.* The FLUXNET2015 dataset and the ONEFlux processing pipeline for eddy covariance data. *Sci. Data* **7**, 1–27 (2020).
60. Pastorello, G. *et al.* A new data set to keep a sharper eye on land-air exchanges. *Eos Trans. Am. Geophys. Union Online* **98**, (2017).
61. Friedl, M. A. *et al.* MODIS Collection 5 global land cover: Algorithm refinements and characterization of new datasets. *Remote Sens. Environ.* **114**, 168–182 (2010).
62. da Silva, P. F. *et al.* Seasonal patterns of carbon dioxide, water and energy fluxes over the Caatinga and grassland in the semi-arid region of Brazil. *J. Arid Environ.* **147**, 71–82 (2017).
63. Griffis, T. J. *et al.* Hydrometeorological sensitivities of net ecosystem carbon dioxide and methane exchange of an Amazonian palm swamp peatland. *Agric. For. Meteorol.* **295**, 108167 (2020).
64. Yuan, F. *et al.* Evaluation and improvement of the E3SM land model for simulating energy and carbon fluxes in an Amazonian peatland. *Agric. For. Meteorol.* **332**, 109364 (2023).
65. Dold, C., Wacha, K., Sauer, T., Hatfield, J. & Prueger, J. Measured and simulated carbon dynamics in Midwestern US corn-soybean rotations. *Glob. Biogeochem. Cycles* **35**,

e2020GB006685 (2021).

66. Miniat, C. F. *et al.* The Coweeta Hydrologic Laboratory and the Coweeta Long-Term Ecological Research Project. *Hydrol. Process.* **35**, e14302 (2021).

67. Denham, S. O. *et al.* The rate of canopy development modulates the link between the timing of spring leaf emergence and summer moisture. *J. Geophys. Res. Biogeosciences* e2022JG007217 (2023).

68. Hollinger, D. *et al.* Multi-decadal carbon cycle measurements indicate resistance to external drivers of change at the Howland Forest AmeriFlux site. *J. Geophys. Res. Biogeosciences* **126**, e2021JG006276 (2021).

69. Fernandez, I. J., Rustad, L. E. & Lawrence, G. B. Estimating total soil mass, nutrient content, and trace metals in soils under a low elevation spruce-fir forest. *Can. J. Soil Sci.* **73**, 317–328 (1993).

70. Nelson, J. A., Carvalhais, N., Migliavacca, M., Reichstein, M. & Jung, M. Water-stress-induced breakdown of carbon–water relations: indicators from diurnal FLUXNET patterns. *Biogeosciences* **15**, 2433–2447 (2018).